GRAIN-SIZE AND DISCHARGE CONTROLS ON SUBMARINE-FAN DEPOSITIONAL PATTERNS FROM FORWARD STRATIGRAPHIC MODELS

Nicolas Hawie[1], Jacob A. Covault[2], and Zoltan Sylvester[2]

[1]*Beicip Franlab, Rueil-Malmaison, France*

[2]*Bureau of Economic Geology, Jackson School of Geosciences, The University of Texas at Austin, Austin, TX, USA*

ABSTRACT

Submarine fans are important components of continental margins; they contain a stratigraphic record of environmental changes and host large accumulations of oil and gas. The grain size and volume of sediment supply to fans is thought to control the heterogeneity of deep-water deposits; predicting spatial variability of sandy and muddy deposits is an important applied challenge in the characterization of fans. Here, we use DionisosFlow stratigraphic-forward models to evaluate the sensitivity of submarine-fan deposition to a range of grain sizes, with corresponding diffusion coefficients ranging from 10 to 100 km^2/kyr for coarse sand to silt/clay, and discharges. In general, finer grains are transported farther in our models because they have larger diffusion coefficients. Coarser grains typical of a sand-rich fan tend to pile up and compensationally stack at the mouth of a proximal feeder channel. Finer grains tend to be distributed across the model domain; however, finer load resulted in fewer channel avulsions because finer sediment did not build topography as high as coarser sediment. Increasing sediment-gravity-flow discharge resulted in a thicker depositional system; however, relatively coarse sediment piled up at the mouth of the feeder channel, which created a slope that promoted basinward sediment transport. Our modeling

results can be applied to predict the overall geometry, stacking, and grain-size distribution of submarine fans. Improved understanding of grain-size and discharge controls also informs interpretation of the stratigraphic record of submarine fans. For example, outcrop observations of heterogeneity and compensational stacking of depocenters can be quantitatively related to changing boundary conditions, namely changes in the caliber and overall supply of sediment delivery to deep-water basin margins.

INTRODUCTION

Submarine fans are deep-water depositional systems that received terrigenous sediment from canyons and channels that extend across continental margins (Piper and Normark, 2001). The deposits of fans host a relatively complete and readily dated record of environmental changes, including tectonic deformation and climate, in their upstream sedimentary systems compared to onshore records (Clift et al., 2000; Clift and Gaedicke, 2002; Romans et al., 2016). The deposits of fans are also globally significant oil and gas reservoirs (Weimer and Pettingill, 2007). The reservoir properties of sandy architectural elements of submarine fans and their lateral continuity and vertical connectivity are important issues for petroleum geology (Piper and Normark, 2001). Piper and Normark (2001) suggested that the distribution of sandy architectural elements is primarily controlled by grain size and sediment supply, and the overall geometry of submarine fans is influenced by basin setting. However, a quantitative understanding of the depositional response of submarine fans to changes in grain size and sediment supply remains elusive.

Forward stratigraphic modeling can be applied to predict the location and heterogeneity of depositional systems and petroleum reservoirs (Miller et al., 2008), as well as the depositional response to controlling factors (Piper and Normark, 2001). For example, in an exploration scenario with low-resolution seismic-reflection data (generally two-dimensional, 2-D, profiles with frequencies of 5-20 Hz; Normark et al., 1993; Prather et al., 2012) and no lithologic control from well penetrations, seismic-stratigraphic interpretation and structural restoration can be applied to create a paleotopographic surface for modeling the location, size, shape, and sub-seismic heterogeneity and stacking of deposits (Deville et al., 2015; Hawie et al., 2015; Barabasch et al., 2018). Commonly used geostatistical methods in reservoir modelling use semivariograms, geometric parameters, and/or training images to reproduce spatial statistics from available seismic-reflection and well data (Pyrcz and Deutsch, 2014). Recently, stratigraphic-forward modeling has been used to incorporate quantitative, process-based geologic information to constrain reservoir modeling. For example, Sacchi et al. (2016) used a depth-averaged flow in the 2-D horizontal plane, basin-scale stratigraphic-forward model called SimClast (Dalman and Weltje, 2008, 2011) to simulate fluvio-deltaic stratigraphic evolution and create a 3-D probability distribution of facies proportions. This probability cube was used as additional input for a geostatistical reservoir model. Similarly, Falivene et al. (2014) improved DionisosFlow basin-scale stratigraphic-forward model predictions of stratigraphic trap and reservoir presence by calibrating the models to independent constraints, such as thicknesses from seismic-reflection or well data.

Hawie et al. (2018) used DionisosFlow at finer temporal and spatial resolution (i.e., 10^3-10^4 yr time steps within an area of 17 km x 17 km with cell sizes of 200 m x 200 m) to simulate the stratigraphic evolution and sub-seismic heterogeneity of a Pleistocene submarine fan on the continental slope of tectonically active eastern Trinidad (Fig. 1). A regional seismic-stratigraphic horizon was used as an initial paleotopographic surface input to the forward stratigraphic model. Over a range of time steps, compensational-stacking patterns governed the lateral continuity and vertical connectivity of sandy and muddy architectural elements of the submarine fan (Hawie et al., 2018); similar compensational stacking patterns in fans are common in other settings (e.g., Deptuck et al., 2008). However, in all models of Hawie et al. (2018), thicknesses in the proximal areas of the models exceeded thicknesses observed in the field.

Here, we revise the reference-case forward stratigraphic model of Hawie et al. (2018) to achieve a better thickness match with the field example offshore Trinidad. Then, we evaluate the sensitivity of this model to input variables, namely: diffusion coefficients related to a range of grain sizes and sediment-gravity-flow discharges. We use an automated multi-simulation workflow using a Latin Hypercube Experimental Design (McKay et al., 1979) with quantitative thickness calibration to quantify the variance of thickness and sand distribution, which can be applied to de-risk petroleum-reservoir presence. Our forward stratigraphic models provide quantification of the influence of key controlling factors, namely grain size, with corresponding diffusion coefficients ranging from 10 to 100 km^2/kyr for coarse sand to silt/clay, and sediment supply (Piper and Normark, 2001), on fan deposition. Understanding controls can be applied to the interpretation of fan stratigraphy in outcrops and subsurface datasets (e.g., Burgess et al., 2019).

GEOLOGIC SETTING

The Columbus foreland-basin system, offshore eastern Trinidad, was created as a result of oblique subduction of the South American plate beneath the eastward migrating Caribbean plate since the Miocene (Leonard, 1983; Weber et al., 2001; Huyghe et al., 2004; Garciacaro et al., 2011a; 2011b) (Fig. 2). Transpression along the Central Range fault zone created a fold-thrust belt in Trinidad (Escalona and Mann, 2011). The offshore expression of the Central Range fault zone is the northwest-southeast-oriented Darien ridge, which defines the boundary between the

Columbus basin and the Barbados accretionary wedge on the slope offshore of eastern Trinidad (Wood and Mize-Spansky, 2009; Moscardelli et al., 2012). The Darien ridge and related fold-thrust structures form highs on the present seafloor that locally exhibit >100 m of relief (Garciacaro et al., 2011a; 2011b; Moscardelli et al., 2012). Fold-thrust-belt deformation and tectono-sedimentary loading of Miocene-Pliocene sediment from the Orinoco river-delta system promoted mud diapirism and the development of northeast-southwest-oriented mud-volcano ridges on the seafloor (up to several hundreds of meters of relief) and shallow subsurface of the slope offshore of eastern Trinidad (Sullivan, 2005; Garciacaro et al., 2011a; 2011b; Moscardelli et al., 2012). High-relief fold-thrust structures and mud volcanoes influence the pathways of down-slope sediment dispersal and the resulting stratigraphic architecture comprising mass-transport deposits and submarine canyon-channel-fan systems offshore of eastern Trinidad (Brami et al., 2000; Moscardelli et al., 2006; Wood and Mize-Spansky, 2009). Northwest-southeast-trending normal faults dominate the Columbus basin shelf and upper slope and accommodate local depocenters (Moscardelli et al., 2006).

PREVIOUS WORK

Hawie et al. (2018) used seismic-reflection horizons from the tectonically active continental slope east of the Columbus basin and along the southern margin of the Barbados accretionary wedge (the ‘NW’ depocenter between the Darien and Haydn ridges in block 25A offshore of Trinidad; Brami et al., 2000; Wood and Mize-Spansky, 2009) to define the top and base of a submarine fan (Fig. 3). They simulated the evolution of this fan (124.5-24.5 ka) with a series of DionisosFlow forward stratigraphic models within a domain of 17 km x 17 km (200 m x 200 m cell sizes), and assessed the impact of duration of time step (20 kyr, 10 kyr, 5 kyr, and 1 kyr) on sub-seismic stacking and heterogeneity of leveed-channel and lobe architectural elements (Fig. 1). They used the regional seismic-reflection horizon at the base of the fan, which overlies mass-transport deposits mapped by Moscardelli et al. (2006), as the initial topography of the model (Fig. 3A). A single 300-600 m-wide feeder channel was located in the south of the model domain; it delivered grain sizes ranging from silt/clay to coarse sand. No differential subsidence was used in the model. Hawie et al. (2018) simulated the transport of relatively coarse grains: 20% coarse sand, 30% medium sand, 40% fine sand, and 10% silt/clay. The transport parameters used for the reference-case model ranged from 10-100 km^2/kyr for water-driven diffusion (or, in the case of submarine fans, sediment-gravity-flow-driven diffusion; K_w) and 0.001-0.1 km^2/kyr for slope-driven transport (K_s).

In all of the models of Hawie et al. (2018), varying the simulated time step (20 kyr, 10 kyr, 5 kyr, and 1 kyr) resulted in a similar thickness trend and compensational stacking of depocenters. All models showed three to four major phases of sediment diversion during the migration of a relatively coarse depocenter. Moreover, the overall proximal-to-distal trend from relatively coarse leveed-channel to finer lobe deposits was similar in all models. However, the proximal and distal areas of all the models exhibited significant thickness differences, locally greater than two-fold, compared to the field (Fig. 3D). In light of this previous work, we are motivated to explore two questions: 1) How can we achieve a better thickness match between model and field cases? 2) Furthermore, how do variable diffusion coefficients related to a range of grain sizes and discharges influence submarine-fan depositional patterns (Piper and Normark, 2001)?

METHODS

Forward Stratigraphic Modeling

DionisosFlow software is a 4-D process-based deterministic multi-lithology forward stratigraphic model that simulates basin filling (Granjeon, 1997; Granjeon and Joseph, 1999; Granjeon, 2014). A range of sedimentary processes are modeled including diffusive sediment transport, delta autoretreat, incision, large-scale avulsion, and slope failure in response to tectonic, climate, and sea-level fluctuations during millennia and longer time scales (e.g., Pinheiro-Moreira, 2000; Rabineau et al., 2005; Alzaga-Ruiz et al., 2009; Gvirtzman et al., 2014; Harris et al., 2016; Hawie et al., 2017). Detailed fluid dynamics are not considered in this model; the goal is to simulate the large-scale (10^2-10^3 m cell size) and long-term (10^3-10^5 yr time steps) evolution of basin fill.

Sediment transport equations are used to simulate the transport of various classes of grain size (e.g., clay to sand) across a basin. This stratigraphic model combines 1) linear slope-driven diffusion (transport proportional to slope), referred to as hillslope creep, and 2) non-linear water- and slope-driven diffusion, referred to as water-discharge-driven transport (Willgoose et al., 1991; Tucker and Slingerland, 1994; Granjeon, 1997; Granjeon and Joseph, 1999; Deville et al., 2015):

$$Q_s = -\left(K_s/\vec{\nabla}h + K_w Q_w^m S^n\right) \text{ (Eq. 1)}$$

where Q_s is sediment discharge (km^3/Myr), K_s and K_w are the slope- and water-driven diffusion coefficients, respectively (km^2/kyr), Q_w is water discharge (m^3/s), n and m are exponents that affect sediment transport capacity with values between 1 and 2 (Tucker and Slingerland, 1994), S is the dimensionless local gradient of the basin, and h (m) is topographic elevation (Granjeon, 2014). Sedimentation and erosion rates are quantified by a mass balance equation in 3-D for each class of grain size (Euzen et al., 2004). Sediment-gravity flows, commonly turbidity currents, are the primary agents of sediment transport, erosion, and deposition in submarine fans (Bouma et al., 1985). We liken the water-driven diffusion coefficient and the water discharge to a sediment-gravity-flow-driven diffusion coefficient and gravity-flow discharge, respectively, which govern the rate of sediment transport though the system. Choosing K_w values for different grain sizes is a challenge because published values span orders of magnitude and they depend on many factors in addition to grain size, such as lithology, roundness, and discharge (Rivenaes, 1992; Falivene et al., 2014; Gvirtzman et al., 2014; Harris et al., 2016). Following Hawie et al. (2018), we used a range of K_w from 10 to 100 km^2/kyr for coarse sand to silt/clay. In a recent publication using DionisosFlow to simulate sedimentation across a larger region offshore Trinidad, Deville et al. (2017) used a range of K_w from 100 to 1000 km^2/kyr. They used much larger K_w values because they simulated sediment transport and deposition across a much larger area (1200 x 1200 km); moreover, their individual cell sizes are nearly the size of our entire model domain (Deville et al., 2017). Deville et al. (2017) required much larger diffusion coefficients than our experiments in order to transport sediment across the entire Barbados accretionary wedge. Ideally, we would tune diffusion coefficients to produce similar geometries and grain-size distribution of deposits (Harris et al., 2014). We created a reference-case model during an initial phase of model calibration. In lieu of grain-size information confirmed by well penetrations, we tuned the variables of the diffusion equation, K_w and Q_w, to achieve a thickness trend that is similar to the published seismic-stratigraphic interpretation of Hawie et al. (2018).

Experimental Designs

In order to achieve a better thickness match between model and the Trinidad field case of Hawie et al. (2018), we manually generated simulations of various grain sizes (i.e., sand- versus silt/clay-rich) during 10 kyr time steps. We slightly modified some of the other input variables of Hawie et al. (2018), such as the discharges and diffusion coefficients (Table 1). We extended the model domain 5 km to the south (17 km wide x 22 km long) to better match the feeder-channel location observed in the seismic-reflection data (Figs. 4 and 5). Once we improved the thickness match with the field case of Hawie et al. (2018), we tested two experimental designs: 1) 80%-20% silt/clay proportion (22 simulations) and 2) +/-20% gravity-flow discharge (22 simulations). We performed multiple automated simulations in CougarFlow using a Latin Hypercube Experimental Design to quantify the standard deviations of thickness and sand-depositional patterns. Latin Hypercube Experimental Design samples variables from uniform distributions and ensures that the ensemble of samples is representative of the natural variability of the system, contrary to simple random sampling in Monte Carlo studies (McKay et al., 1979). In statistical sampling, a square grid containing sample positions is a Latin square if there is only one sample in each row and each column. A Latin Hypercube is the generalization of this concept to an arbitrary number of variables, whereby each sample is the only one in each axis-aligned hyperplane containing it. When sampling a function of N variables, the range of each variable is divided into M equally probable intervals. M sample points are then placed to satisfy the Latin Hypercube requirements; this forces the number of intervals, M, to be equal for each variable. The maximum number of combinations for a Latin Hypercube of N variables and M intervals can be computed with the following equation (McKay et al., 1979; Audze and Eglais, 1977; Iman et al., 1980; 1981):

$$\left(\prod_{n=0}^{M-1}(M-n)\right)^{N-1} = (M!)^{N-1} \text{ (Eq. 2)}$$

The following are features of Latin Hypercube Experimental Design: 1) it treats every variable as equally important and ensures uniformly distributed sampling; 2) it samples the full range of a variable; 3) it allows for multiple, multidimensional variables (e.g., 1-D sediment load and/or 3-D topographic variables); and 4) we, the designers, determine the number of simulations, which include output grids of properties for comparison to a reference case (Hawie et al., 2015).

Some caveats to our experimental designs include: 1) we restricted our model domain to the submarine fan, excluding the upstream canyon-channel system; and 2) we opened the northern boundary of the model and closed the eastern and western boundaries. Focusing only on the submarine fan required us to strongly vary diffusion coefficients in order to achieve a fan shape (e.g., Hawie et al., 2018). For example, more diffusion is required to produce the relatively flat, sheet-like geometries of the distal fan.

RESULTS

We improved the thickness match between our manually calibrated stratigraphic-forward model and the field case of Hawie et al. (2018) by modifying the grain-size inputs to be 5% coarse sand (10 km^2/kyr), 10% medium sand (15 km^2/kyr), 30% fine sand (30 km^2/kyr), and 55% silt/clay (100 km^2/kyr) (Fig. 4B). This grain-size distribution is more similar to mud-rich continental margins (e.g., Reading and Richards, 1994), such as offshore Trinidad, compared to the relatively sand-rich models of Hawie et al. (2018). Approximately 1/3 of the total sediment load was transported beyond the northern boundary of the model, and ~80% of this sediment load was silt/clay. Although we improved the thickness match, especially in the proximal and central parts of the model domain, with model-thickness values >75% of the field case, there is still a mismatch in the western and thinner, peripheral parts of the model (~30%-60% of the field case). The overall architecture of the model is similar to the models of Hawie et al. (2018): compensationally stacked proximal leveed-channel depositional elements transition downstream to lobes (Figs. 4C and 5; Supplementary Animations 1, 2). The model output shows at least four phases of depocenter migration (Figs. 4C and 5; Supplementary Animations 1, 2). Initially, the depocenter was oriented southwest-to-northeast (0.124–0.104 Ma), then it shifted to the west and was oriented more south-to-north (0.104–0.094 Ma), followed by a more gradual shift to the east (0.094-0.064 Ma), where it split into three channels covering the model domain, and it was predominantly oriented southwest-to-northeast at the end of the simulation (0.054-0.024 Ma) (Fig. 4C; Supplementary Animations 1, 2).

Following this initial phase of manual calibration, we implemented the two experimental designs in CougarFlow. In the first experimental design, we varied silt/clay load, hereafter simply called mud load, 80%-20%. Figures 6 and 7 show the thicknesses and the distributions of coarse and medium sand in the maximum and minimum mud-load simulations (Supplementary Animations 3-6). Lower mud load results in relatively thick accumulations in the northeast distal part of the model domain, immediately downstream from the feeder channel; higher mud load results in a relatively thick band across the northern, central, and eastern regions of the model (Fig. 8A). Higher mud load also results in fewer major depocenters (at least three) compared to lower mud load (at least six major depocenters) (Figs. 6 and 7; Supplementary Animations 3-6). The map of thickness standard deviation of the 22 simulations shows larger variance in thickness (+/- nearly 20 m) near the proximal feeder channel (Fig. 8C). The thickness standard deviation is also greater along channel forms extending to the northeast away from the feeder channel (Fig. 8C). At first glance, the coarse and medium sand proportion maps look similar in both the high and low mud-load simulations (Figs. 6 and 7). However, the map of sand proportion standard deviation shows large variance (+/- >10%) along the boundaries of the model domain, especially the southeastern boundary (Fig. 8E).

In the second experimental design, we varied the sediment-gravity-flow discharge +/-20% relative to the manually calibrated model. Figures 9 and 10 show the thicknesses and the distributions of coarse and medium sand in the maximum (+20%) and minimum (-20%) discharge simulations (Supplementary Animations 7-10). Discharge appears to play a significant role in thickness difference, with nearly uniformly greater thickness corresponding with higher discharge (Fig. 11A). In detail, higher discharge results in fewer major depocenters (at least two to three dominant depocenter- and channel-orientation directions) compared to lower discharge (similar to the manually calibrated model, at least four or five major depocenters) (Figs. 9 and 10; Supplementary Animations 7-10). Moreover, the largest difference in thickness, with excess thickness in the case of higher discharge, is observed in the most proximal and distal parts of the model (Fig. 11A). The map of thickness standard deviation of the 22 simulations shows larger variance (+/- nearly 20 m) in the central region of the model domain, extending from the proximal feeder channel basinward to the northern distal part (Fig. 11C). As in the first experimental design, the coarse and medium sand proportion maps look similar in both the maximum and minimum discharge simulations (Figs. 9 and 10). The map of sand proportion standard deviation of the 22 simulations shows larger variance (+/- nearly 10%) along the northwestern region of the model domain (Fig. 11E).

Interpretations

Improved Model-Field Match

We improved the thickness match between our manually calibrated stratigraphic-forward model and the field case of Hawie et al. (2018) by modifying the grain-size inputs to be finer (Fig. 4). In our modeling, sediment discharge is a function of the diffusion coefficient K_w (Eq. 1), which is larger for smaller grain sizes (Table 1). So, larger grain sizes assigned smaller K_w values will tend to pile up at the mouth of the feeder channel, like in the models of Hawie et al. (2018). By significantly modifying the grain sizes in our new manually calibrated model to be finer, with correspondingly larger K_w values, the sediment-transport equations of the model diffused sediment farther across the model domain and achieved a better match with the field. Similar to Hawie et al. (2018), the model shows repeated cycles of channel avulsion, compensational stacking, and unconfined deposition at the mouths of channels (e.g., Sun et al., 2010). In particular, compensational stacking is a key characteristic of submarine-fan deposits (e.g., Deptuck et al., 2008), and our results show that relatively simple diffusion-based models can produce realistic compensation patterns. In our model, topographic build up by deposition promotes compensation and depocenter migration around the model domain. However, the thickness of compensationally stacked depocenters in the proximal region of the model, near the feeder channel, is less pronounced than in the models of Hawie et al. (2018). This is because our new model comprises relatively fine grains with larger diffusion coefficients, which are more easily transported over topography and generate an overall smoother, more elongate fan geometry.

Experimental Design 1: Grain Size

The first experimental design highlights the influence of changes in diffusion coefficients related to a range of grain sizes on fan deposition (Figs. 6-8; Supplementary Animations 3-6). In the higher-mud-load case, the more widely distributed, relatively thick band of deposits across the northern, central, and eastern regions of the model results from the larger diffusion coefficient K_w (Eq. 1) of finer sediment compared to the lower-mud-load case (Fig. 8A). The larger diffusion coefficient promotes the basinward transport of finer sediment across the model. In the lower-mud-load case, coarser sediment piles up at the mouth of the feeder channel, which creates a steeper proximal slope that bypasses sediment to the distal northeast part of the model (Fig. 8A). The higher-mud-load case results in fewer major depocenters because mud transport is less sensitive to topography and generates lower slopes than the lower-mud-load (i.e., sandier) case. As diffusion is predominantly driven by slope and the diffusion coefficient, lower slopes and higher diffusion coefficients will promote more unconfined spreading of deposits rather than more topographically directed (i.e., confined), compensationally stacked deposits. The difference in depocenters in the high- versus low-mud-load cases is also reflected in the map of sand proportion standard deviation, where the largest variance in thicknesses of the 22 simulations is at the mouth of the feeder channel in the proximal, central region of the model domain (Fig. 8C). Here, relatively coarse depocenters are variably shifting depending on mud load (i.e., the low-mud-load case shifts about twice as often as the high-mud-load case; compare Figs. 6 and 7). The largest variance in sand proportions of the 22 simulations is located along the boundaries of the model domain (Fig. 8E). This is because sandy depocenters did not visit those regions of the model in every simulation.

Experimental Design 2: Discharge

The second experimental design highlights the influence of sediment-gravity-flow discharge on fan deposition (Figs. 9-11; Supplementary Animations 7-10). Intuitively, higher discharge (+ 20%) results in a thicker depositional system (Fig. 11A). However, higher discharge results in fewer major depocenters because, initially, voluminous relatively coarse sediment accumulates in front of the proximal feeder channel and builds up a slope that dominates the direction of sediment transport during the simulation. The buildup of a slope in the proximal region of the model promotes bypass of finer sediment to the distal region, thereby causing some of the largest thickness differences between the high and low discharge cases along a region extending from the proximal feeder channel basinward to the northern distal part of the model (Fig. 11A). Moreover, the largest variance in thicknesses of the 22 simulations is along this north-to-south region, where thickness probably depends on whether high enough discharge promotes the development of a single major north-to-south depocenter, as in the higher discharge case (Fig. 11C). The large variance in sand proportions of the 22 simulations is located in the northwest because sandy depocenters did not visit that region of the model domain in every simulation (Fig. 11E). In contrast, the central region is immediately down slope of the proximal feeder channel and consistently received the bulk of the relatively coarse sediment load. Mud transport is less sensitive to topography and, as a result, can more easily spread across the model.

DISCUSSION

The primary goals of our experiments were to quantify and understand the submarine-fan depositional response to changes in diffusion coefficients related to a range of grain sizes and discharges. In the models of Hawie et al. (2018), thicknesses in proximal areas exceeded thicknesses observed in the field. We increased the proportion of mud (i.e., silt/clay), with correspondingly larger K_w values, to the model by a factor of 5.5 in order to improve the thickness match between our reference-case model and the field case of Hawie et al. (2018). Rather than sand piling up in the proximal region of the model, at the mouth of the feeder channel, a mixed sediment load was more uniformly distributed across the model. Indeed, this is consistent with general models of submarine-fan run-out based on their mud- versus sand-rich sediment supply (e.g., Reading and Richards, 1994; Richards et al., 1998). Some of the largest, longest run-out submarine fans in the world are characterized as mud rich with highly “efficient” sediment transport (Richards et al., 1998; and references therein). That said, some of these general models of submarine-fan systems are qualitative classification schemes; our modeling provides some quantitative constraints on fan run-out and depositional patterns associated with grain size of sediment supply. Finer grain sizes are transported farther in our model; this has also been demonstrated for deposition on natural submarine-fan systems, such as the Amazon fan (Pirmez and Imran, 2003), and supported by simple models of sediment transport and deposition using an advection-settling scheme (Straub et al., 2008; and references therein). For example:

$$x = U\frac{z_i}{w_s} \text{ (Eq. 3)}$$

where the distance the particle travels (x) is equal to the velocity of the particle (U) multiplied by the of the initial height of the particle above the bed (z_i) divided by the particle settling velocity (w_s). Although this advection-settling scheme is different than how Eq. 1 diffuses sediment across our model domain, it supports our experimental results that show, in general, keeping all other variables constant, a finer, slower settling grain will be transported a longer distance compared to a coarser, faster settling grain.

We also explored an experimental design of variable mud load (80%-20%). Cases of larger mud load resulted in fewer channel avulsions and, consequently, fewer depocenters. Finer sediment does not build topography as high as coarser sediment. Lower-relief topography and lower slopes inhibit large-scale shifts in the position of depocenters, which can remain stable for long periods. In contrast, decreasing mud load (i.e., increasing sand load) resulted in more avulsions and the active migration of the depocenter across the model. This is consistent with conceptual models of sandy submarine fans based on outcrops and high-resolution, shallow-subsurface data in tectonically active settings; they tend to have limited channel extension and more frequent avulsions associated with steep basin-margin slopes (Hoyal et al., 2014). These concepts have been further developed in physical experiments (e.g., Spinewine et al., 2009; Hamilton et al., 2015; Postma et al., 2016) and reduced-complexity modeling of submarine-fan evolution over an evolving topography (e.g., Burgess et al., 2019). Although our models do not capture the high-resolution detail of morphodynamic interaction between flow and topography as in some physical experiments, including a potentially important hydraulic jump flow transformation and resultant depositional architecture (Mutti and Normark, 1987), our models show sandier sediment supply associated with the general trend of more frequent avulsions resulting in a larger number of depocenters.

Increasing sediment-gravity-flow discharge had the intuitive result of overall thicker deposits. However, this also resulted in fewer depocenters because relatively coarse sediment piled up at the mouth of the feeder channel, which created a slope that promoted basinward sediment transport along a dominant south-to-north fairway. Piper and Normark (2001), in their analysis of the distribution of sandy and muddy architectural elements of submarine fans, interpreted that steepening of proximal channels promotes basinward sand bypass and the development of a pattern of sand distribution similar to detached lobes of Mutti (1979), with lobe deposition displaced from the limit of sandy channel deposition. Although this interpretation was related to depositional patterns of channels and lobes in response to avulsions on the Amazon fan (Pirmez and Flood, 1995), steeper channels appear to promote basinward sediment bypass in our models as well.

Our modeling results can be applied to predict the overall geometry, stacking, and grain-size distribution of submarine-fan oil and gas reservoirs. In tectonically active, stepped-slope profiles, like offshore eastern Trinidad, increasing sand delivery to deep water (e.g., Moscardelli et al., 2012), can result in more compensational stacking of relatively sand-rich, proximal depocenters (Piper and Normark, 2001). Increasing sediment supply, but maintaining grain-size distribution, can result in basinward sediment transport along a dominant fairway, thereby potentially producing isolated, “detached lobe” depositional architectures downstream of primary feeder channels. Our modeling also informs the interpretation of the depositional record of submarine fans. Observing some of the aforementioned depositional patterns, such as more/less frequent avulsions and compensational stacking of depocenters (e.g., Straub and Pyles, 2012), can be interpreted in the context of changing boundary conditions, namely changes in the caliber and overall supply of sediment to deep water. In order to better understand the results of our modeling experiments, we maintain our input variables (e.g., silt/clay proportion and discharge) as constant for the entire simulation time of 100 kyr. Of course, in nature, boundary conditions change during periods as long as 100 kyr, and future work will follow some of the more recent forward modeling work of Sylvester et al. (2015) and Burgess et al. (2019), which vary inputs, including substrate mobility. We also aim to pursue more numerous simulations, of the order of thousands, in order to achieve better calibration with the subsurface; new developments in high-performance parallelized computing processes can accelerate computations of high-resolution DionisosFlow models by as many as five times (Granjeon et al., 2018).

CONCLUSION

We used DionisosFlow forward stratigraphic models to quantify and understand the submarine-fan depositional response to changes in diffusion coefficients related to a range of grain sizes and discharges. We achieved a thickness match between a reference-case forward stratigraphic model and a field example offshore Trinidad. Finer-grained models resulted in fewer channel avulsions and, consequently, fewer depocenters compared to coarser-grained models. Lower-relief topography and lower slopes of finer-grained models inhibited large-scale shifts in the position of depocenters. In contrast, coarser-grained loads resulted in more avulsions and the active migration of the depocenter across the model domain. This is consistent with general models of submarine-fan run-out based on their mud- versus sand-rich sediment supply (e.g., Reading and

Richards, 1994; Richards et al., 1998). Higher discharge resulted in a thicker depositional system, but fewer channel avulsions because an initial relatively coarse-grained sediment buildup at the mouth of the proximal feeder channel promoted bypass of finer sediment to the distal region of the model domain. Our modeling results can be applied to predict the depositional architecture of submarine fans; changes in diffusion coefficients related to a range of grain sizes and discharges have a measurable effect on the overall geometry, stacking, and heterogeneity of our models. Our results can also be applied to the interpretation of fan stratigraphy in outcrops and subsurface datasets (e.g., Burgess et al., 2019). For example, observations of compensational stacking in outcrops (e.g., Straub and Pyles, 2012) can be related to changes in sediment supply to the depositional system. Our future work will evaluate the depositional response to temporally varying the inputs of more numerous simulations. We envision thousands of simulations to generate facies probability maps to be integrated in reservoir models.

ACKNOWLEDGMENTS

We thank the sponsors of the Quantitative Clastics Laboratory (http://www.beg.utexas.edu/qcl) and Beicip-Franlab for access to DionisosFlow and CougarFlow forward stratigraphic modeling and multi-simulation software. We are grateful for thought-provoking comments and recommendations from Tim Demko and Mauricio Perillo.

REFERENCES CITED

Alzaga-Ruiz, H., Granjeon, D., Lopez, M., Seranne, M., & Roure, F. (2009). Gravitational collapse and Neogene sediment transfer across the western margin of the Gulf of Mexico: Insights from numerical models. Tectonophysics, 470(1), 21-41.

Barabasch, J., Ducros, M., Hawie, N., Daher, S. B., Nader, F. H., & Littke, R. (2019). Integrated 3D forward stratigraphic and petroleum system modeling of the Levant Basin, Eastern Mediterranean. Basin Research, 31(2), 228-252.

Bouma, A. H., Normark, W. R., & Barnes, N. E. (1985). Submarine fans and related turbidite systems. SpringerVerlag Inc., Berlin and New York.

Brami, T. R., Pirmez, C., Archie, C., Heeralal, S., & Holman, K. L. (2000). Late Pleistocene deep-water stratigraphy and depositional processes, offshore Trinidad and Tobago. In Deep-water reservoirs of the world: Gulf Coast Section SEPM 20th Annual Research Conference (pp. 104-115).

Burgess, P. M., Masiero, I., Toby, S. C., & Duller, R. A. (2019). A Big Fan of Signals? Exploring Autogenic and Allogenic Process and Product In a Numerical Stratigraphic Forward Model of Submarine-Fan Development. Journal of Sedimentary Research, 89(1), 1-12.

Clift, P., D., & Gaedicke, C. (2002). Accelerated mass flux to the Arabian Sea during the middle to late Miocene. Geology, 30(3), 207-210.

Clift, P. D., Degnan, P., Hannigan, R., & Blusztajn, J. (2000). Sedimentary and geo-chemical evolution of the Dras forearc basin, Indus suture, Ladakh Himalaya, India, Geol. Soc. Am. Bull.,112 (3), 450 – 466.

Dalman, R. A., & Weltje, G. J. (2008). Sub-grid parameterisation of fluvio-deltaic processes and architecture in a basin-scale stratigraphic model. Computers & Geosciences, 34(10), 1370-1380.

Dalman, R. A., & Weltje, G. J. (2012). SimClast: An aggregated forward stratigraphic model of continental shelves. Computers & geosciences, 38(1), 115-126.

Deptuck, M. E., Piper, D. J., Savoye, B., & Gervais, A. (2008). Dimensions and architecture of late Pleistocene submarine lobes off the northern margin of East Corsica. Sedimentology, 55(4), 869-898.

Deville, E., Mascle, A., Callec, Y., Huyghe, P., Lallemant, S., Lerat, O., ... & Loubrieux, B. (2015). Tectonics and sedimentation interactions in the east Caribbean subduction zone: an overview from the Orinoco delta and the Barbados accretionary prism. Marine and Petroleum Geology, 64, 76-103.

Audze, P., & Eglais, V. (1977). New approach to design of experiments. Problems of Dynamics and Strength, 35, 104-107.

Escalona, A., & Mann, P. (2011). Tectonics, basin subsidence mechanisms, and paleogeography of the Caribbean-South American plate boundary zone. Marine and Petroleum Geology, 28(1), 8-39.

Euzen, T., Joseph, P., Du Fornel, E., Lesur, S., Granjeon, D., & Guillocheau, F. (2004). Three-dimensional stratigraphic modelling of the Grès d'Annot system, Eocene-Oligocene, SE France. Geological Society, London, Special Publications, 221(1), 161-180.

Falivene, O., Frascati, A., Gesbert, S., Pickens, J., Hsu, Y., & Rovira, A. (2014). Automatic calibration of stratigraphic forward models for predicting reservoir presence in exploration. AAPG Bulletin, 98(9), 1811-1835.

French, C. D., & Schenk, C. J. (2004). Map showing geology, oil and gas fields, and geologic provinces of the Caribbean region. US Geological Survey, Central Energy Resources Team, https://pubs.usgs.gov/of/1997/ofr-97-470/OF97-470K/index.html.

Garciacaro, E., Mann, P., & Escalona, A. (2011a). Regional structure and tectonic history of the obliquely colliding Columbus foreland basin, offshore Trinidad and Venezuela. Marine and Petroleum Geology, 28(1), 126-148.

Garciacaro, E., Escalona, A., Mann, P., Wood, L., Moscardelli, L., & Sullivan, S. (2011b). Structural controls on Quaternary deepwater sedimentation, mud diapirism, and hydrocarbon distribution within the actively evolving Columbus foreland basin, eastern offshore Trinidad. Marine and Petroleum Geology, 28(1), 149-176

Granjeon, D. (1997). Modélisation stratigraphique déterministe: conception et applications d'un modéle diffusif 3 D multilithologique. PhD dissertation, Université de Rennes.

Granjeon, D. (2014). 3D forward modelling of the impact of sediment transport and base level cycles on continental margins and incised valleys. Depositional Systems to Sedimentary Successions on the Norwegian Continental Margin: International Association of Sedimentologists, Special Publication, 46, 453-472.

Granjeon, D., Have., P., Coatleven, J., Pegaz-Fiornet, S., & Chauveau, B. (2018). High Performance Stratigraphic Modeling of Shelf to Deep-Water Plays. Search and Discovery Article 11122. AAPG 2018 Annual Convention and Exhibition, Salt Lake City, Utah, USA, May 20-23-2018.

Granjeon, D., & Joseph, P. (1999). Concepts and applications of a 3-D multiple lithology, diffusive model in stratigraphic modeling. Numerical experiments in stratigraphy: Recent advances in stratigraphic and sedimentologic compouter simulations: SEPM Special Publication, 62, 197-210.

Gvirtzman, Z., Csato, I., & Granjeon, D. (2014). Constraining sediment transport to deep marine basins through submarine channels: The Levant margin in the Late Cenozoic. Marine Geology, 347, 12-26.

Hamilton, P. B., Strom, K. B., & Hoyal, D. C. (2015). Hydraulic and sediment transport properties of autogenic avulsion cycles on submarine fans with supercritical distributaries. Journal of Geophysical Research: Earth Surface, 120(7), 1369-1389.

Harris, A. D., Covault, J. A., Madof, A. S., Sun, T., Sylvester, Z., & Granjeon, D. (2016). Three-Dimensional Numerical Modeling of Eustatic Control On Continental-Margin Sand Distribution. Journal of Sedimentary Research, 86(12), 1434-1443.

Hawie, N., Deschamps, R., Granjeon, D., Nader, F. H., Gorini, C., Müller, C., & Baudin, F. (2017). Multi-scale constraints of sediment source to sink systems in frontier basins: a forward stratigraphic modelling case study of the Levant region. Basin Research, 29(S1), 418-445.

Hawie, N., Covault, J. A., Dunlap, D., & Sylvester, Z. (2018). Slope-fan depositional architecture from high-resolution forward stratigraphic models. Marine and Petroleum Geology, 91, 576-585.

Hoyal, D. C. H., Demko, T., Postma, G., Wellner, R. W., Pederson, K., Abreu, V., ... & Strom, K. (2014). Evolution, architecture and stratigraphy of Froude supercritical submarine fans. In American Association of Petroleum Geologists Annual Convention and Exhibition, April (pp. 6-9).

Huyghe, P., Foata, M., Deville, E., Mascle, G., & Caramba Working Group. (2004). Channel profiles through the active thrust front of the southern Barbados prism. Geology, 32(5), 429-432.

Iman, R. L., Davenport, J. M., & Zeigler, D. K. (1980). Latin hypercube sampling (program user's guide). Department of Energy, Sandia Laboratories.

Iman, R. L., Helton, J. C., & Campbell, J. E. (1981). An approach to sensitivity analysis of computer models: Part I—Introduction, input variable selection and preliminary variable assessment. Journal of quality technology, 13(3), 174-183.

Leonard, R. (1983). Geology and hydrocarbon accumulations, Columbus Basin, offshore Trinidad. AAPG Bulletin, 67(7), 1081-1093.

McKay, M. D., Beckman, R. J., & Conover, W. J. (1979). Comparison of three methods for selecting values of input variables in the analysis of output from a computer code. Technometrics, 21(2), 239-245.

Miller, J. K., Sun, T., Li, H., Stewart, J., Genty, C., Li, D., & Lyttle, C. (2008, January). Direct modeling of reservoirs through forward process-based models: can we get there?. In International petroleum technology conference. International Petroleum Technology Conference.

Mize, K. L. (2004). Controls on the Morphology and Development of Deep-Marine Channels, Eastern Offshore Trinidad and Venezuela. MS Thesis, The University of Texas at Austin.

Moscardelli, L., & Wood, L. (2008). New classification system for mass transport complexes in offshore Trinidad. Basin research, 20(1), 73-98.

Moscardelli, L., Wood, L., & Mann, P. (2006). Mass-transport complexes and associated processes in the offshore area of Trinidad and Venezuela. AAPG bulletin, 90(7), 1059-1088.

Moscardelli, L., Wood, L. J., & Dunlap, D. B. (2012). Shelf-edge deltas along structurally complex margins: a case study from eastern offshore Trinidad. AAPG bulletin, 96(8), 1483-1522.

Mutti, E. (1979). Turbidites et cones sous-marins profonds. Sédimentation détritique (fluviatile, littorale et marine), 1, 353-419.

Normark, W. R., Posamentier, H., & Mutti, E. (1993). Turbidite systems: state of the art and future directions. Reviews of Geophysics, 31(2), 91-116.

Pinheiro-Moreira, J. L. (2000). Stratigraphie sismique et modélisation stratigraphique des dépôts de l'Éocène du Bassin de Santos (marge brésilienne). PhD dissertation, Université de Rennes.

Piper, D. J., & Normark, W. R. (2001). Sandy fans--from Amazon to Hueneme and beyond. AAPG bulletin, 85(8), 1407-1438.

Pirmez, C., & Flood, R. D. (1995). Morphology and structure of Amazon Channel. In Proceedings of the Ocean Drilling Program. Initial Reports (Vol. 155, pp. 23-45). Ocean Drilling Program.

Pirmez, C., & Imran, J. (2003). Reconstruction of turbidity currents in Amazon Channel. Marine and petroleum geology, 20(6-8), 823-849.

Postma, G., Hoyal, D. C., Abreu, V., Cartigny, M. J., Demko, T., Fedele, J. J., ... & Pederson, K. H. (2016). Morphodynamics of supercritical turbidity currents in the channel-lobe transition zone. In Submarine Mass Movements and their Consequences (pp. 469-478). Springer International Publishing.

Prather, B. E., Pirmez, C., & Winker, C. D. (2012). Stratigraphy of linked intraslope basins: Brazos-Trinity system western Gulf of Mexico. Application of the Principles of Seismic Geomorphology to Continental-Slope and Base-of-Slope Systems: Case Studies from Seafloor and Near-Seafloor Analogues: SEPM, Special Publication, 99, 83-110.

Pyrcz, M. J., & Deutsch, C. V. (2014). Geostatistical reservoir modeling. Oxford university press.

Rabineau, M., Berné, S., Aslanian, D., Olivet, J. L., Joseph, P., Guillocheau, F., ... & Granjeon, D. (2005). Sedimentary sequences in the Gulf of Lion: a record of 100,000 years climatic cycles. Marine and Petroleum Geology, 22(6), 775-804.

Reading, H. G., & Richards, M. (1994). Turbidite systems in deep-water basin margins classified by grain size and feeder system. AAPG bulletin, 78(5), 792-822.

Richards, M., Bowman, M., & Reading, H. (1998). Submarine-fan systems I: characterization and stratigraphic prediction. Marine and Petroleum Geology, 15(7), 689-717.

Rivenaes, J. C. (1992). Application of a dual-lithology, depth-dependent diffusion equation in stratigraphic simulation. Basin Research, 4(2), 133-146.

Romans, B. W., Castelltort, S., Covault, J. A., Fildani, A., & Walsh, J. P. (2016). Environmental signal propagation in sedimentary systems across timescales. Earth-Science Reviews, 153, 7-29.

Ryan, W. B., Carbotte, S. M., Coplan, J. O., O'Hara, S., Melkonian, A., Arko, R., ... & Bonczkowski, J. (2009). Global multi-resolution topography synthesis. Geochemistry, Geophysics, Geosystems, 10(3).

Sacchi, Q., Borello, E. S., Weltje, G. J., & Dalman, R. (2016). Increasing the predictive power of geostatistical reservoir models by integration of geological constraints from stratigraphic forward modeling. Marine and Petroleum Geology, 69, 112-126.

Spinewine, B., Sequeiros, O. E., Garcia, M. H., Beaubouef, R. T., Sun, T., Savoye, B., & Parker, G. (2009). Experiments on wedge-shaped deep sea sedimentary deposits in minibasins and/or on channel levees emplaced by turbidity currents. Part II. Morphodynamic evolution of the wedge and of the associated bedforms. Journal of Sedimentary Research, 79(8), 608-628.

Straub, K. M., Mohrig, D., McElroy, B., Buttles, J., & Pirmez, C. (2008). Interactions between turbidity currents and topography in aggrading sinuous submarine channels: A laboratory study. GSA Bulletin, 120(3-4), 368-385.

Sullivan, S. M. (2005). Geochemistry, sedimentology, and morphology of mud volcanoes, eastern offshore Trinidad. MS thesis, The University of Texas at Austin.

Sun, T., Ghayour, K., Hall, B., & Miller, J. (2010, December). Process-based modeling of deep water depositional systems. In Seismic Imaging of Depositional and Geomorphic Systems: Gulf Coast Section SEPM Foundation 30th Annual Bob F. Perkins Research Conference (pp. 88-112).

Sylvester, Z., Cantelli, A., & Pirmez, C. (2015). Stratigraphic evolution of intraslope minibasins: Insights from surface-based model. AAPG Bulletin, 99(6), 1099-1129.

Tucker, G. E., & Slingerland, R. L. (1994). Erosional dynamics, flexural isostasy, and long-lived escarpments: A numerical modeling study. Journal of Geophysical Research: Solid Earth, 99(B6), 12229-12243.

Weber, J. C., Dixon, T. H., DeMets, C., Ambeh, W. B., Jansma, P., Mattioli, G., ... & Pérez, O. (2001). GPS estimate of relative motion between the Caribbean and South American plates, and geologic implications for Trinidad and Venezuela. Geology, 29(1), 75-78.

Weimer, P., & Pettingill, H. S. (2007). Deep-water exploration and production: A global overview. Atlas of deep-water outcrops: AAPG Studies in Geology, 56.

Willgoose, G., Bras, R. L., & Rodriguez-Iturbe, I. (1991). A coupled channel network growth and hillslope evolution model: 1. Theory. Water Resources Research, 27(7), 1671-1684.

Wood, L. J & Mize-Spansky, K. L. (2009). Quantitative seismic geomorphology of a Quaternary leveed-channel system, offshore eastern Trinidad and Tobago, northeastern South America. AAPG Bulletin, 93(1), 101-125.

FIGURE CAPTIONS

Figure 1. Reference-case model (10 kyr time step) of Hawie et al. (2018). (A) Isochore map of the entire model. (B) Cross sections of the model. Left (L) and right (R) orientations in cross sections are left and right in map in part (A). Cross-section locations are indicated in part A. (C) Isochore maps of depositional sequences within the model showing major phases of sediment diversion.

Figure 2. Caribbean geologic setting. Bathymetry is from Geomapapp.org (Ryan et al., 2009). Faults are black lines (French and Schenk, 2004).

Figure 3. (A-B) Time-structure maps of base and top of the slope fan in block 25A, offshore Trinidad (Hawie et al., 2018). (A) Base of the slope fan is the initial bathymetry of the stratigraphic forward model (Top MTC_1 horizon of Moscardelli et al., 2006). (B) Top of the slope fan is the seafloor (Mize, 2004; Sullivan, 2005; Moscardelli and Wood, 2008; Wood and Mize-Spansky, 2009). (C) Isochron map of the slope fan from Moscadelli et al. (2006) and Moscardelli and Wood (2008). (D) Difference in thickness between the model and the slope fan in block 25A, offshore Trinidad (Hawie et al., 2018).

Figure 4. New extended reference-case model. (A) isochore map of the new model. (B) Difference in thickness of the model and the slope fan in block 25A, offshore Trinidad (Hawie et al., 2018). (C) Isochore maps of depositional sequences within the model showing major phases of sediment diversion.

Figure 5. Cross sections of the new extended reference-case model. Left (L) and right (R) orientations in cross sections are left and right in map in Figure 4A.

Figure 6. (A) Isochore map of the high mud load model. (B) Coarse and medium sand percentage within the model. (C) Proximal, medial and distal cross sections showing the coarse sand content in the model. Left (L) and right (R) orientations in cross sections are left and right in maps. Cross-section locations are indicated in part A.

Figure 7. (A) Isochore map of the low mud load model. (B) Coarse and medium sand percentage within the model. (C) Proximal, medial and distal cross sections showing the coarse sand content in the model. Left (L) and right (R) orientations in cross sections are left and right in maps. Cross-section locations are indicated in part A.

Figure 8. (A) Difference in thickness between the high and low mud load models. (B-E) CougarFlow simulation results. (B) Average of thicknesses. (C) Standard deviation of thicknesses. (D) Average of coarse and medium sand percentages. (E) Standard deviation of coarse and medium sand percentages.

Figure 9. (A) Isochore map of the high discharge model. (B) Coarse and medium sand percentage within the model. (C) Proximal, medial and distal cross sections showing the coarse sand content in the model. Left (L) and right (R) orientations in cross sections are left and right in maps. Cross-section locations are indicated in part A.

Figure 10. (A) Isochore map of the low discharge model. (B) Coarse and medium sand percentage within the model. (C) Proximal, medial and distal cross sections showing the coarse sand content in the model. Left (L) and right (R) orientations in cross sections are left and right in maps. Cross-section locations are indicated in part A.

Figure 11. (A) Difference in thickness between the high and low discharge models. (B-E) CougarFlow simulation results. (B) Average of thicknesses. (C) Standard deviation of thicknesses. (D) Average of coarse and medium sand percentages. (E) Standard deviation of coarse and medium sand percentages.

TABLE CAPTIONS

Table 1. Reference-case model inputs.

Table 1.

Model Size	17 x 22 km
Cell Size	200 x 200 m
Duration	124.5-24.5 ka
Time Step	10 kyr
Sediment Discharge	215 km^3/Myr
Grain size Classes	5% coarse sand (0.5 mm)
	10 % medium sand (0.3 mm)
	30% fine sand (0.125 mm)
	55% silt/clay (0.004 mm)
Water Discharge	65 m^3/s
K_w	10 km^2/kyr coarse sand
	15 km^2/kyr medium sand
	30 km^2/kyr fine sand
	100 km^2/kyr silt/clay
K_s	0.018 km^2/kyr coarse sand
	0.014 km^2/kyr medium sand
	0.012 km^2/kyr fine sand
	0.001 km^2/kyr silt/clay

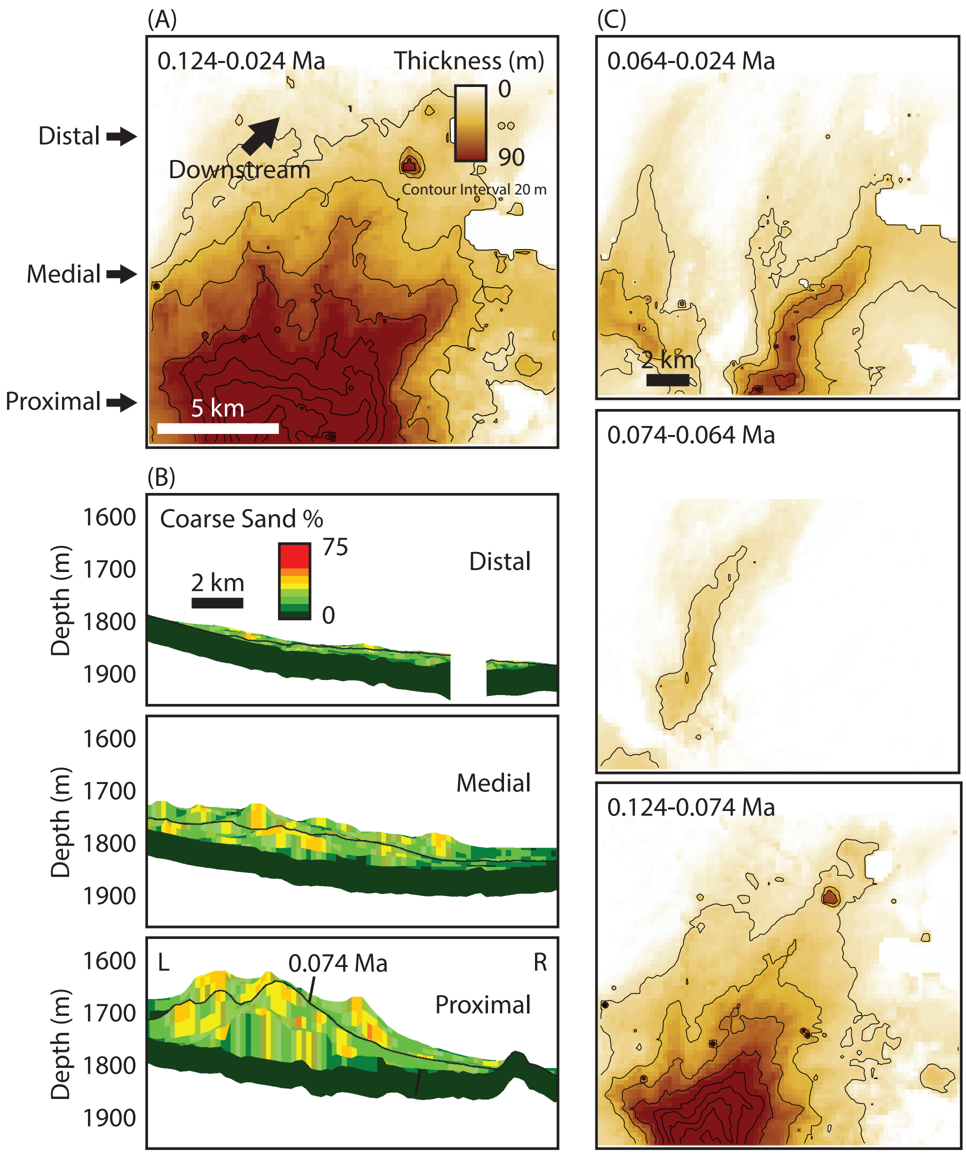
(A)
0.124-0.024 Ma
Thickness (m)
0
90
Contour Interval 20 m
Downstream
Distal
Medial
Proximal
5 km
(B)
Coarse Sand %
75
0
2 km
Distal
Medial
Proximal
L
R
0.074 Ma
Depth (m)
1600
1700
1800
1900
(C)
0.064-0.024 Ma
2 km
0.074-0.064 Ma
0.124-0.074 Ma

Figure 1

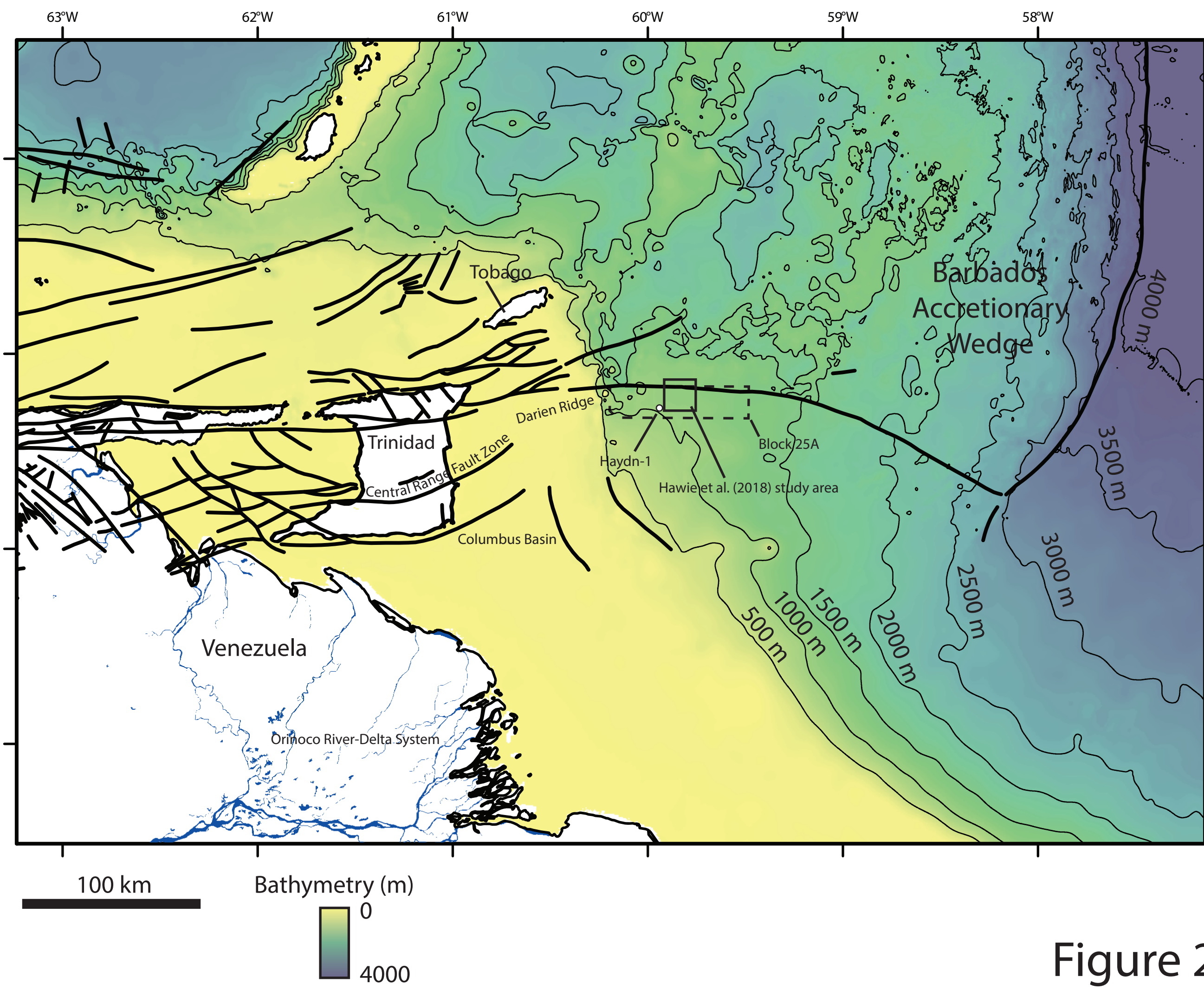

63°W
62°W
61°W
60°W
59°W
58°W
12°N
11°N
10°N
9°N
Tobago
Barbados Accretionary Wedge
4000 m
Darien Ridge
Trinidad
Central Range Fault Zone
Haydn-1
Block 25A
Hawie et al. (2018) study area
Columbus Basin
3500 m
3000 m
2500 m
2000 m
1500 m
1000 m
500 m
Venezuela
Orinoco River-Delta System
100 km
Bathymetry (m)
0
4000

Figure 2

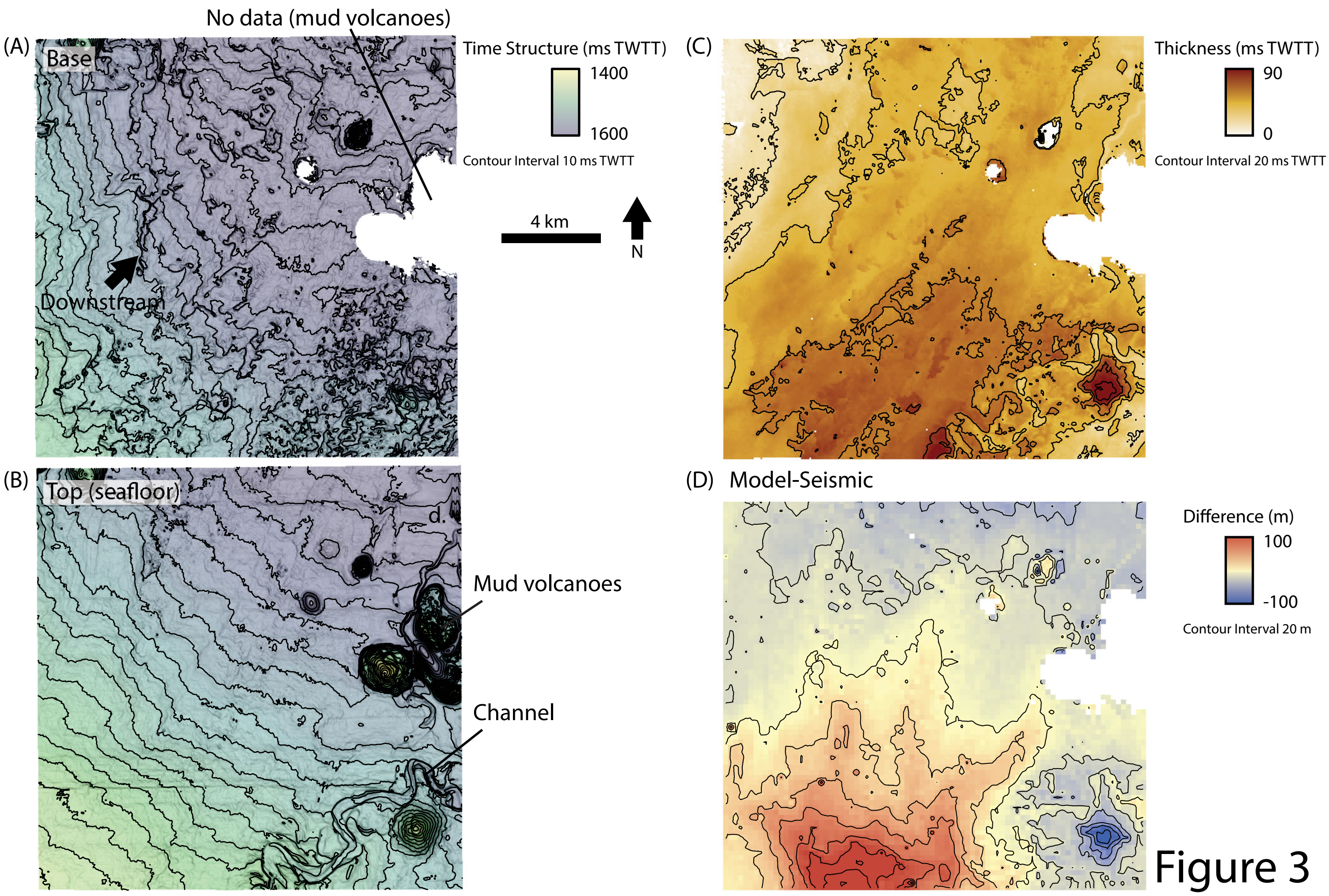

No data (mud volcanoes)
(A)
Base
Downstream
Time Structure (ms TWTT)
1400
1600
Contour Interval 10 ms TWTT
4 km
N
(C)
Thickness (ms TWTT)
90
0
Contour Interval 20 ms TWTT
(B)
Top (seafloor)
d.
Mud volcanoes
Channel
(D)
Model-Seismic
Difference (m)
100
-100
Contour Interval 20 m

Figure 3

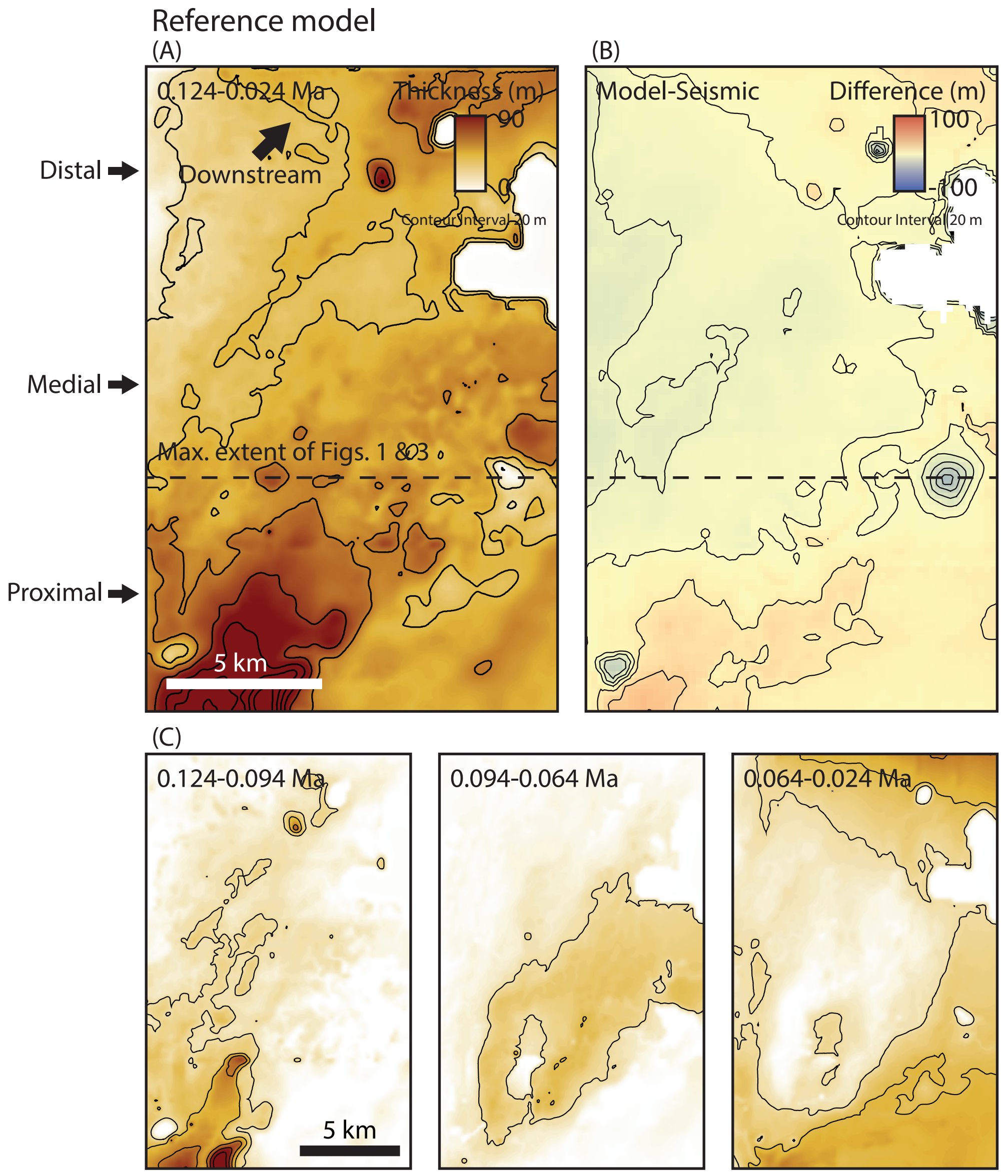
Reference model
(A)
0.124-0.024 Ma
Thickness (m)
90
0
Downstream
Contour Interval 20 m
Distal
Medial
Proximal
Max. extent of Figs. 1 & 3
5 km
(B)
Model-Seismic
Difference (m)
100
-100
Contour Interval 20 m
(C)
0.124-0.094 Ma
0.094-0.064 Ma
0.064-0.024 Ma
5 km

Figure 4

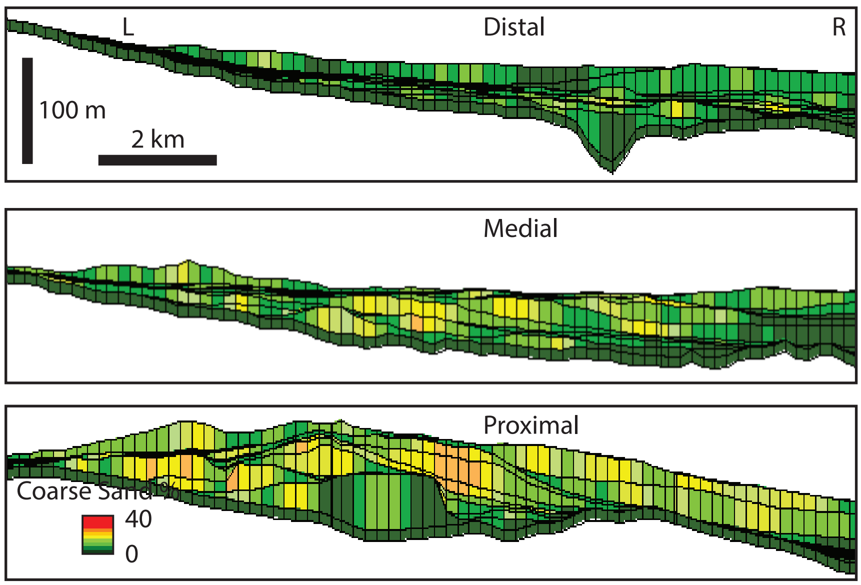

Figure 5

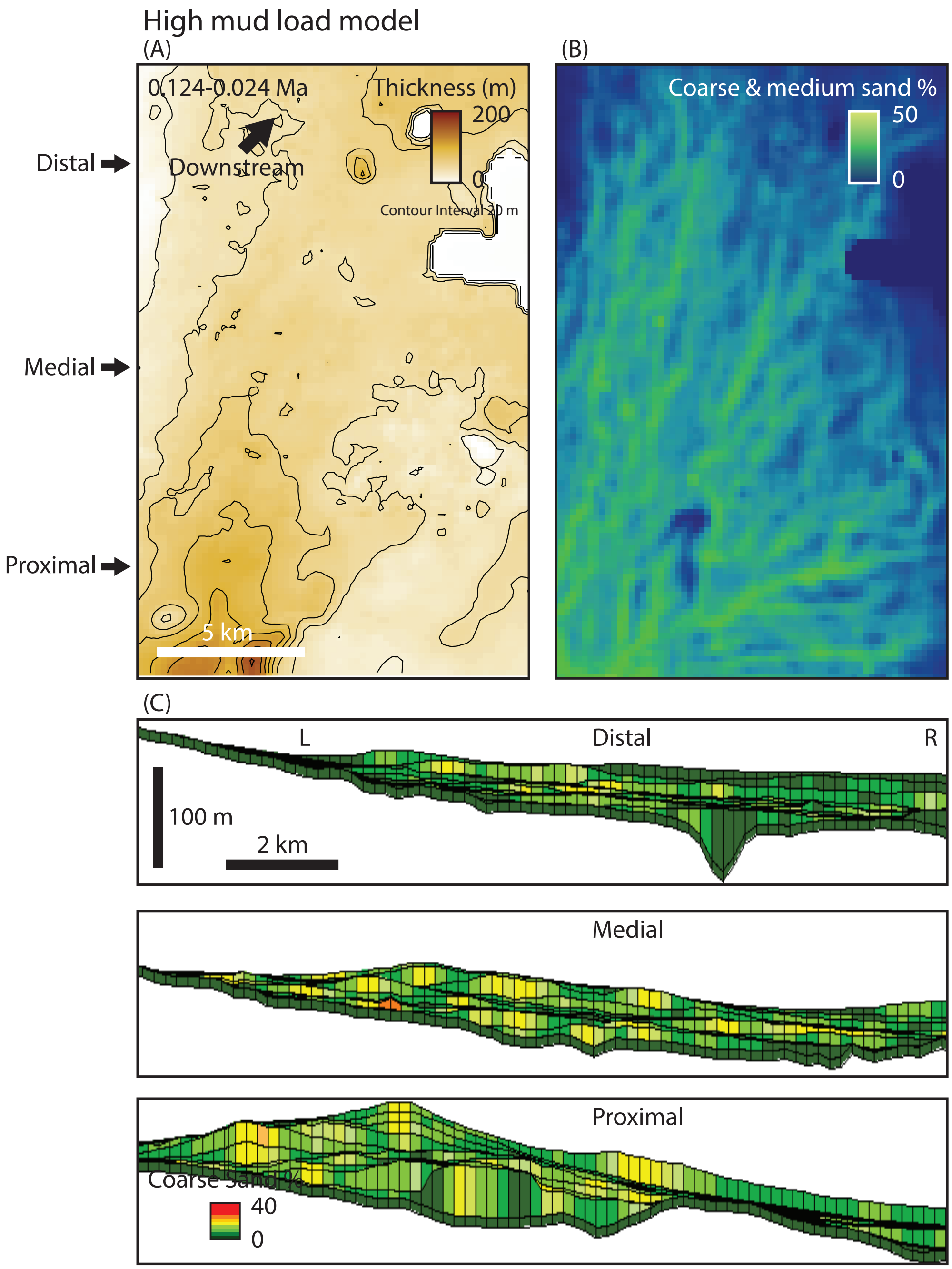
High mud load model
(A)
0.124-0.024 Ma
Thickness (m)
200
0
Downstream
Contour Interval 20 m
5 km
Distal
Medial
Proximal
(B)
Coarse & medium sand %
50
0
(C)
L
Distal
R
100 m
2 km
Medial
Proximal
40
0

Figure 6

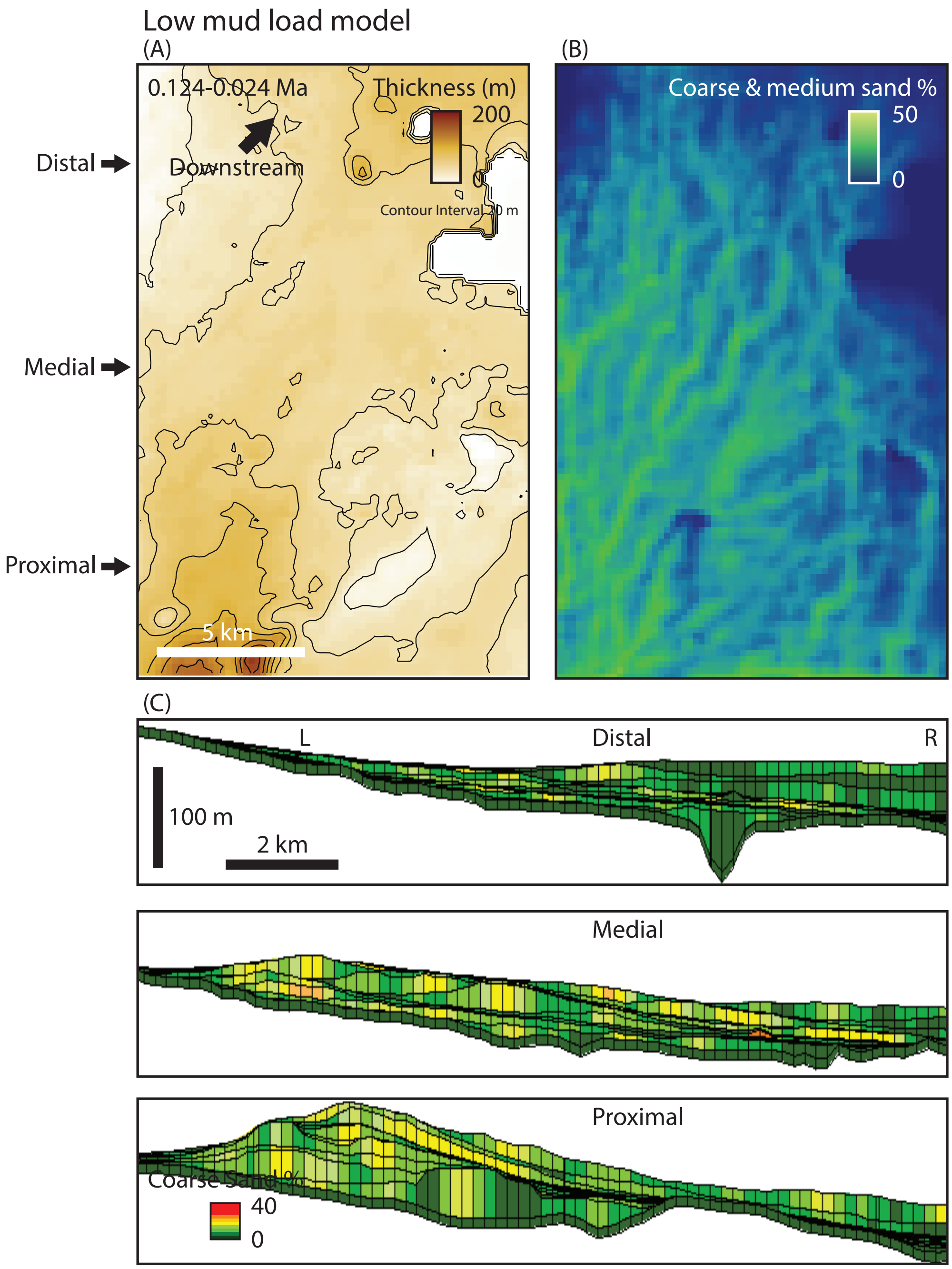
Low mud load model
(A)
(B)
0.124-0.024 Ma
Thickness (m)
200
Downstream
Contour Interval 20 m
Distal
Medial
Proximal
5 km
Coarse & medium sand %
50
0
(C)
L
Distal
R
100 m
2 km
Medial
Proximal
Coarse Sand %
40
0

Figure 7

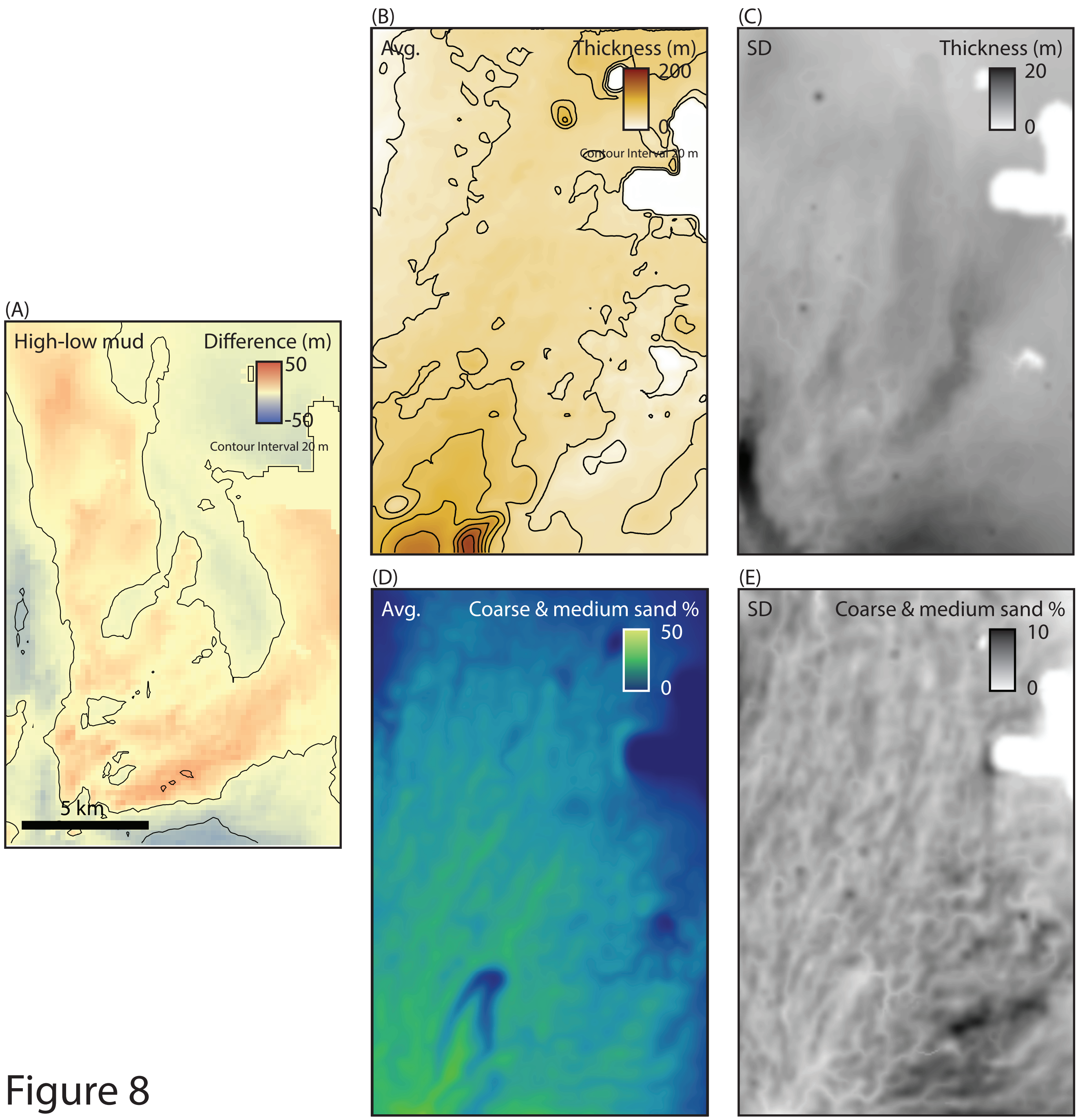
(A)
High-low mud
Difference (m)
50
-50
Contour Interval 20 m
5 km
(B)
Avg.
Thickness (m)
200
0
Contour Interval 20 m
(C)
SD
Thickness (m)
20
0
(D)
Avg.
Coarse & medium sand %
50
0
(E)
SD
Coarse & medium sand %
10
0

Figure 8

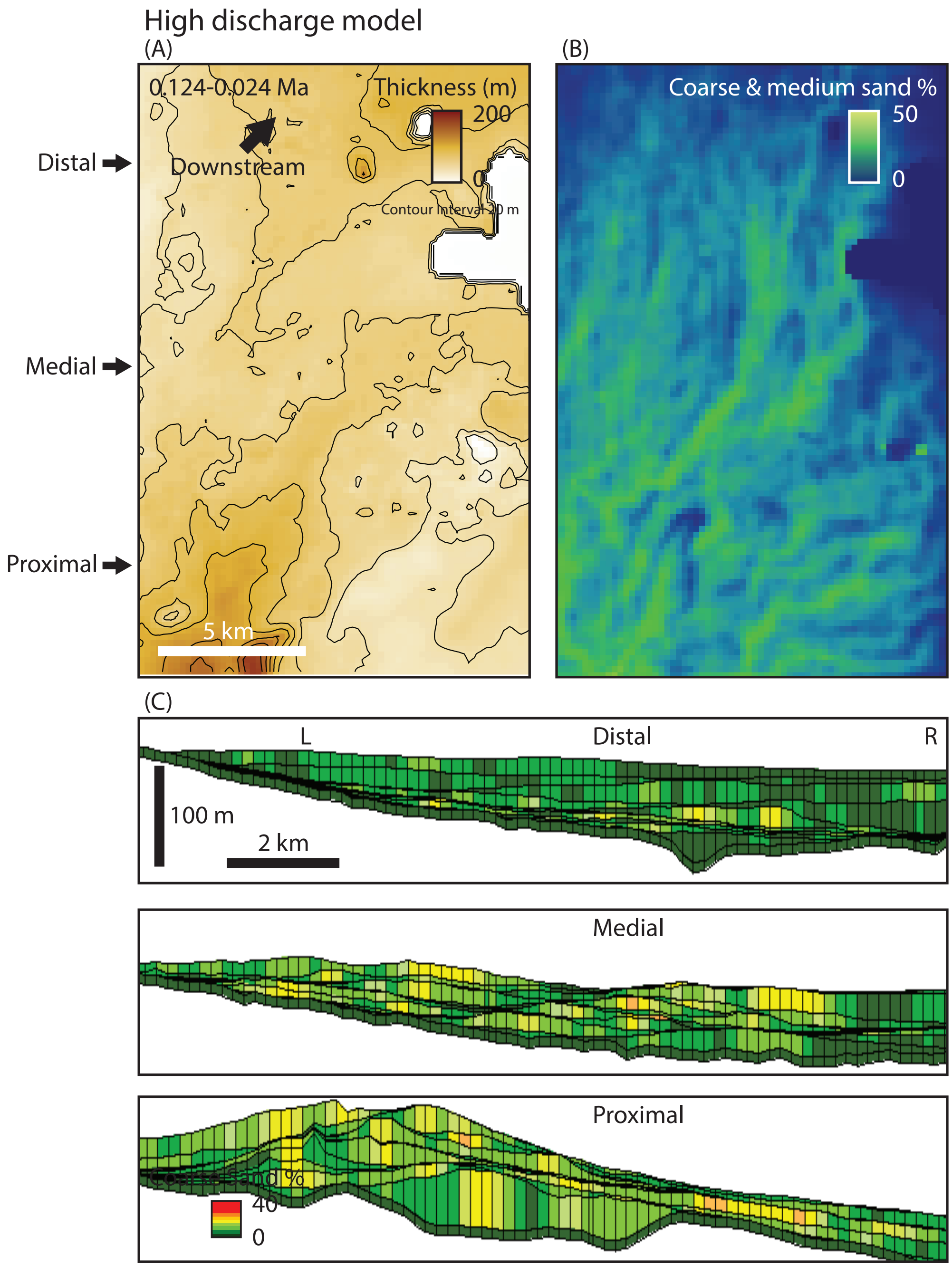

High discharge model
(A)
(B)
0.124-0.024 Ma
Thickness (m)
200
0
Downstream
Contour Interval 20 m
5 km
Distal
Medial
Proximal
Coarse & medium sand %
50
0
(C)
L
Distal
R
100 m
2 km
Medial
Proximal
40
0

Figure 9

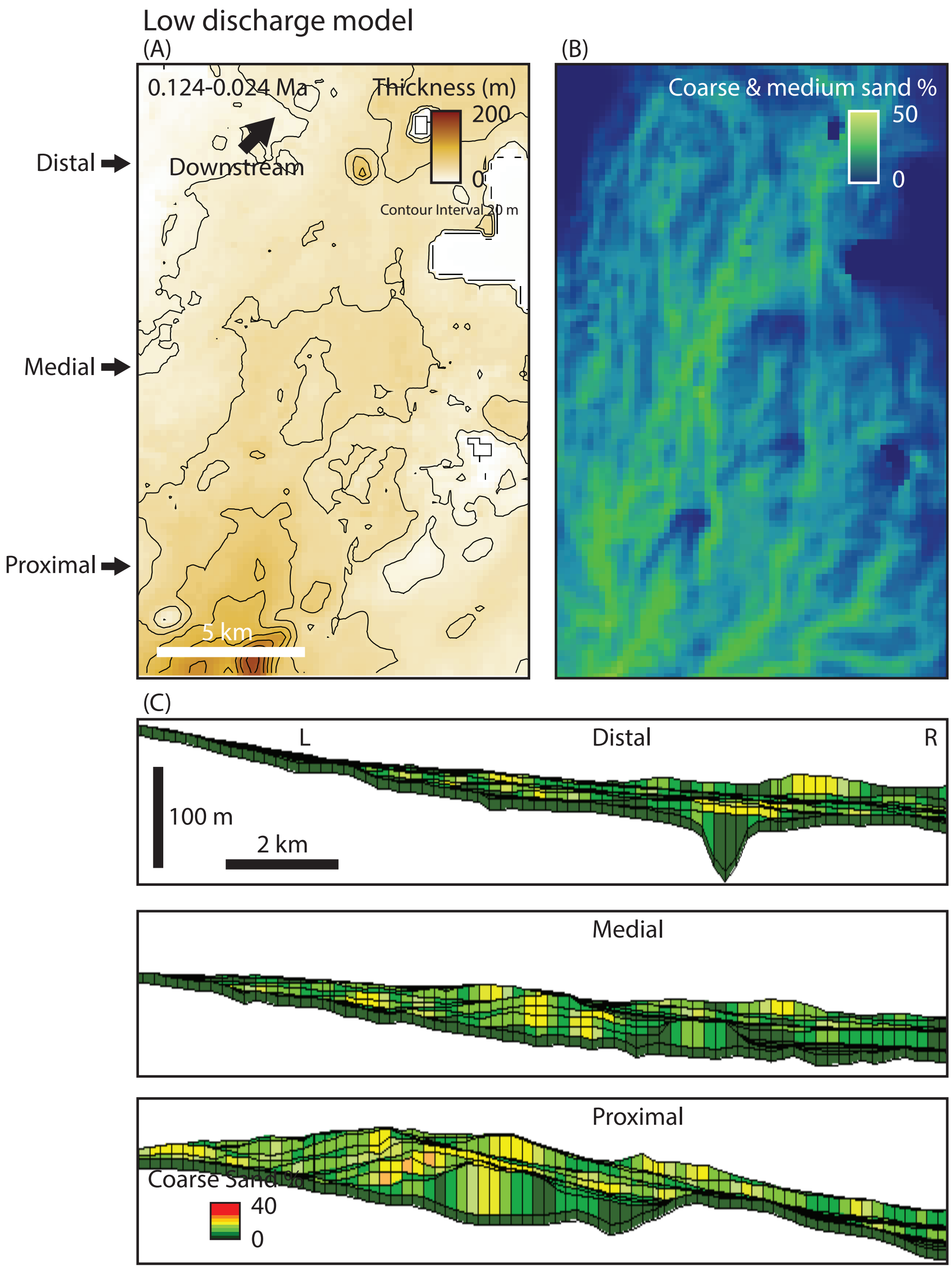

Low discharge model
(A)
(B)
0.124-0.024 Ma
Thickness (m)
200
0
Downstream
Contour Interval 20 m
5 km
Distal
Medial
Proximal
Coarse & medium sand %
50
0
(C)
L
Distal
R
100 m
2 km
Medial
Proximal
40
0

Figure 10

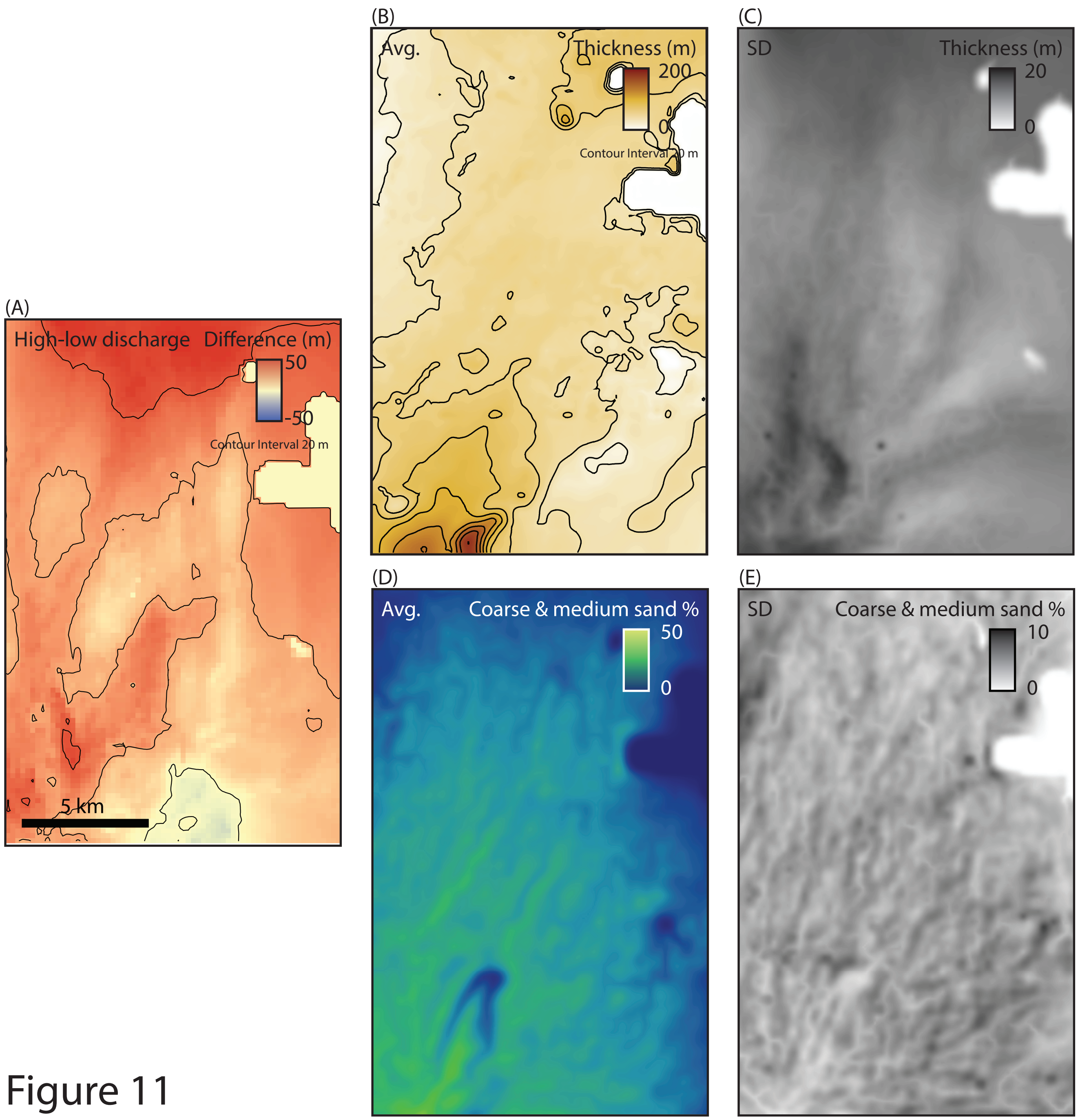
(A)
High-low discharge
Difference (m)
50
-50
Contour Interval 20 m
5 km
(B)
Avg.
Thickness (m)
200
0
Contour Interval 20 m
(C)
SD
Thickness (m)
20
0
(D)
Avg.
Coarse & medium sand %
50
0
(E)
SD
Coarse & medium sand %
10
0

Figure 11